Manipulating Elastic Waves with Conventional Isotropic Materials

Hexuan Gao and Zhihai Xiang*
Department of Engineering Mechanics, Tsinghua University, Beijing 100084, China

(Received 16 July 2018; revised manuscript received 22 April 2019; published 17 June 2019)

Transformation methods have stimulated many interesting applications of manipulating electromagnetic and acoustic waves by using metamaterials, such as super-lens imaging and cloaking. These successes are mainly due to the form-invariant property of the Maxwell equations and acoustic equations. However, the similar progress in manipulating elastic waves is very slow, because the elastodynamic equations are not form invariant. We show that the expression of the elastodynamic potential energy can almost retain its form after conformal mapping, if the longitudinal wave velocity is much larger than the transverse wave velocity, or if the wavelength can be shortened by converting the waves into surface modes. Based on these findings, it is possible to design and fabricate alternative devices with ease to manipulate elastic waves at will. One example presented in this paper is an efficient vibration isolator, which contains a 180-degree wave bender made of conventional rubbers. Compared with a conventional isolator of the same shape, similar static support stiffness, and smaller damping ratio, this isolator can further reduce wave transmissions by up to 39.9 dB in the range of 483–1800 Hz.

DOI: 10.1103/PhysRevApplied.11.064040

I. INTRODUCTION

A popular paradigm to manipulate waves is using the transformation method, which originated in manipulating electromagnetic waves [1,2], and has been extended to other types of waves, such as acoustic waves [3,4], surface water waves [5], and even matter waves [6]. However, in contrast to the great success of transformation optics [7–9] and transformation acoustics [10–12], the progress of transformation elastics is rather slow. This is because the classical elastodynamic equations are generally not form invariant [13], which is the essential prerequisite of transformation methods [1]. To circumvent this difficulty, people have tried to design elastic metamaterials in some special cases, such as the Cosserat type material [14,15], high-frequency approximations [16,17], bending waves in thin plates [18–21], and utilizing the prestresses [22–24]. Unfortunately, it is still very difficult to use any of these special solutions to manipulate broadband low-frequency elastic waves of complex modes [25].

Because of this thorny issue of lack of invariance for elastodynamic equations [9], it is difficult to expect perfect metamaterials to manipulate elastic waves of complex modes. Instead, we can design almost perfect elastic metamaterials based on an idea of minimizing the extra term in the expression of elastic potential energy after transformation. This can be generally achieved by using conformal mapping, requiring the longitudinal wave velocity to be much larger than the transverse wave velocity, and converting the wave into surface modes of slow velocities. Since conformal mapping [2,17,26] is adopted in the design, the metamaterial can be easily fabricated with conventional isotropic materials free of local resonance and has good performance in broad frequency bandwidths. An elastic wave isolator designed in this way will be presented here as an experimental demonstration, which is composed of an aluminum alloy shell and a 180-degree elastic wave bender made of two kinds of conventional rubbers.

This paper is organized as follows. In Sec. II, we present the theoretical derivation of the effective properties of the elastic metamaterial and an index η, which measures the extent of form invariance of potential energy expression after conformal mapping. Based on this theory, we design a vibration isolator in Sec. III. Numerical simulations are also presented to demonstrate its performances. Then, experimental verifications are detailed in Sec. IV. Finally, summaries are given in Sec. V.

II. THEORETICAL BASIS

Transformation methods used to design metamaterials [1,2] usually start from a homogeneous and isotropic material in virtual space. The geometry of this material in virtual space is transformed into the desired geometry of a metamaterial in physical space by using certain coordinate mapping. In this way, a point $\mathbf{x}$ in virtual space is transformed into a point $\mathbf{x}' = \mathbf{x}'(\mathbf{x})$ in physical space. At the same time, field variables in virtual space are also transformed into physical space with a given gauge.

*xiangzhihai@tsinghua.edu.cn

Consequently, by using the change of variables, the governing equations in virtual space are transformed into physical space. If the transformed governing equations have the same forms as those in virtual space, we can easily obtain the effective inhomogeneous material properties of the metamaterial in physical space by comparing the corresponding terms in these two sets of equations. The selection of the gauge connecting the field variables before and after transformation could be arbitrary [15], and has nothing to do with the form invariance of the governing equations [24]. However, this gauge is usually chosen as the deformation gradient $\partial\mathbf{x}'/\partial\mathbf{x}$ [1,2,13], so that the deformed grid in physical space shows the wave trajectories [27] and the transformed elasticity tensor is symmetric [15].

Milton *et al.* have proven that the classic elastodynamic equations are not form invariant [13]. This is also true if using conformal mappings [28]. All existing work on discussing the form invariance of elastodynamic equations involves the complex analysis of the gradient of elasticity tensor, because the metamaterial is inhomogeneous. To avoid this complexity, we focus on the form invariance of the elastic potential energy (integral invariant) instead of the elastodynamic equations (differential invariants) [29] in this paper.

Neglecting the body force, the elastic potential energy in the virtual space of volume V is

$$\Pi = \int_V \frac{1}{2}\varepsilon_{ij}D_{ijkl}\varepsilon_{kl}dV + \int_V \rho\ddot{u}_i u_i dV + \int_V \mu\dot{u}_i u_i dV - \int_{S_T} T_i u_i dS, \tag{1}$$

where $D_{ijkl} = \lambda\delta_{ij}\delta_{kl} + G(\delta_{ik}\delta_{jl} + \delta_{il}\delta_{jk})$ is the component of elasticity tensor with Lamé parameters λ and G; δ_{ij} is the component of Kronecker delta; ε_{ij} is the component of strain tensor; u_i is the component of displacement vector; $T_i = \bar{\sigma}_{ij}n_j$ is the component of given traction vector on boundary S_T with normal vector n_j; $\bar{\sigma}_{ij}$ is the component of stress tensor on boundary S_T; ρ is mass density; μ is the damping factor; and the overhead dot denotes the derivative with respect to time. Here, we use Einstein's notation of index summation. Since conformal mapping will be used in the following, all indices take the value of 1 or 2.

We also use the deformation gradient as the gauge to connect the field variables before and after transformation

$$u_i = u'_j\frac{\partial x'_j}{\partial x_i} \quad \text{and } \bar{\sigma}_{ij} = J\bar{\sigma}'_{kl}\frac{\partial x_k}{\partial x'_i}\frac{\partial x_l}{\partial x'_j}, \tag{2}$$

where $J = \det(\partial x'_j/\partial x_i)$, and all values with superscript prime are defined in physical space. In addition, it is well known that the conformal mapping used for the geometrical transformation has the following properties

$$\frac{\partial x'_k}{\partial x_i}\frac{\partial x'_l}{\partial x_i} = J\delta_{kl} \quad \text{and} \quad \frac{\partial^2 x'_k}{\partial x_i\partial x_i} = 0. \tag{3}$$

Applying the transformation specified in Eqs. (2) and (3) to Eq. (1) and noticing $dV = J^{-1}dV'$, $n_j dS = J^{-1}(\partial x'_i/\partial x_j)n'_i dS'$, $T'_i = \bar{\sigma}'_{ij}n'_j$, and $\varepsilon_{ij} = (\partial u_i/\partial x_j + \partial u_j/\partial x_i)/2$, we can obtain the transformed elastic potential energy in physical space

$$\Pi' = \int_{V'}\left(\frac{1}{2}J\lambda\varepsilon'_{ii}\varepsilon'_{jj} + JG\varepsilon'_{ij}\varepsilon'_{ij} + E_x\right)dV' + \int_{V'}\rho\ddot{u}'_i u'_i dV' + \int_{V'}\mu\dot{u}'_i u'_i dV' - \int_{S'_T}T'_i u'_i dS', \tag{4}$$

where the extra term is

$$E_x = \frac{G}{J}\left(u'_i u'_j\frac{\partial^2 x'_i}{\partial x_k\partial x_l}\frac{\partial^2 x'_j}{\partial x_k\partial x_l} + 2u'_i\varepsilon'_{rs}\frac{\partial^2 x'_i}{\partial x_k\partial x_l}\frac{\partial x'_r}{\partial x_k}\frac{\partial x'_s}{\partial x_l}\right). \tag{5}$$

Thus, the expression of elastic potential energy is not form invariant either. This coincides with existing findings [13, 28]. We cannot obtain effective material properties of the metamaterial in the physical space by directly comparing Eq. (4) with Eq. (1), unless the contribution of extra term E_x to the strain energy can be neglected. The conditions of ignoring E_x can be found by conducting the following dimensional analysis.

Under harmonic excitation of magnitude a' and wavelength L' at frequency f, the displacement at location $\mathbf{z}' = (x'_1, x'_2)$ can be approximated as $u'_i = a'\,\mathrm{Re}\{\exp[\mathrm{i}(\boldsymbol{\kappa}'\cdot\mathbf{z}' - 2\pi ft)]\}$, where $\boldsymbol{\kappa}'$ is the wave number vector of magnitude $\langle\boldsymbol{\kappa}'\rangle\sim 2\pi/L'$. Since $\varepsilon_{ij} = (\partial u_i/\partial x_j + \partial u_j/\partial x_i)/2$, the magnitude of the strain in physical space is about $\langle\varepsilon'_{ij}\rangle\sim\langle\boldsymbol{\kappa}'\rangle\langle u'_i\rangle$. With all these results and noticing that the velocities of the longitudinal wave and transverse wave are $C'_p = \sqrt{(\lambda' + 2G')/\rho'}$ and $C'_s = \sqrt{G'/\rho'}$, respectively, we can calculate the ratio of the magnitude of traditional strain energy terms over the magnitude of the extra term

$$\eta = \frac{\left\langle\frac{1}{2}J\lambda\varepsilon'_{ii}\varepsilon'_{jj} + JG\varepsilon'_{ij}\varepsilon'_{ij}\right\rangle}{\langle E_x\rangle} = \frac{2\left(\frac{J\pi C'_p}{L'C'_s}\right)^2}{\left\langle\frac{\partial^2 x'_i}{\partial x_k\partial x_l}\right\rangle\left[\left\langle\frac{\partial^2 x'_j}{\partial x_k\partial x_l}\right\rangle + \frac{4\pi}{L'}\left\langle\frac{\partial x'_r}{\partial x_k}\frac{\partial x'_s}{\partial x_l}\right\rangle\right]}. \tag{6}$$

If $\eta \gg 1$, the potential energy is almost form invariant

$$\Pi' \approx \int_{V'} \left(\frac{1}{2} J\lambda \varepsilon'_{ii}\varepsilon'_{jj} + JG\varepsilon'_{ij}\varepsilon'_{ij}\right) dV' + \int_{V'} \rho \ddot{u}'_i u'_i dV' + \int_{V'} \mu \dot{u}'_i u'_i dV' - \int_{S'_T} T'_i u'_i dS'. \tag{7}$$

In this case, the material properties of the metamaterial in physical space can be obtained by comparing Eq. (7) with Eq. (1) as

$$\lambda' = J\lambda, \quad G' = JG, \quad \rho' = \rho, \quad \mu' = \mu. \tag{8}$$

III. REALIZING A VIBRATION ISOLATOR

A. Effective material properties of the wave bender

With the theory presented in Sec. II, it is possible to design many interesting elastic metamaterials. We just give a simple example in this paper, a wave bender, for demonstration.

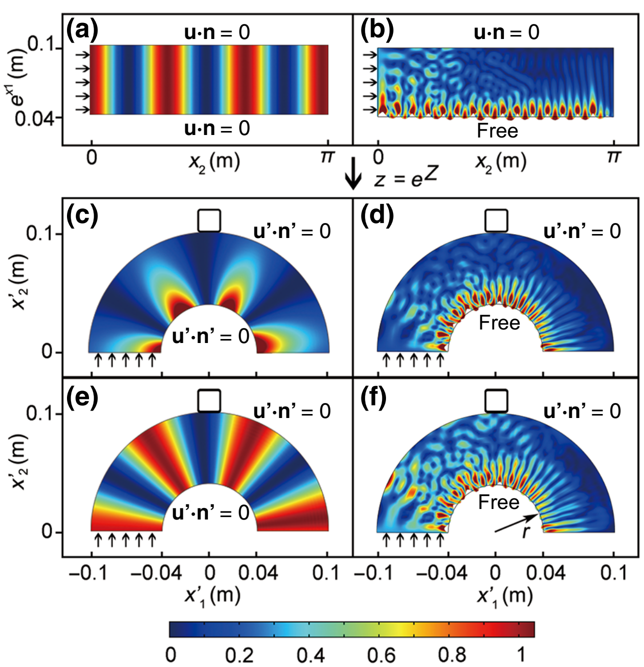

FIG. 1. Snap shots of the total displacement field $\sqrt{u_1'^2 + u_2'^2}$ (normalized to the amplitude of the incident wave). (a) The virtual space with normal constraints on the upper and the lower boundaries ($f = 10\,000$ Hz). (b) The virtual space with normal constraint only on the upper boundary ($f = 1000$ Hz). (c) The physical space transformed from (a). (d) The physical space transformed from (b). (e) The modified total displacement field $\sqrt{J}\sqrt{u_1'^2 + u_2'^2}$ of (c). (f) The modified total displacement field $\sqrt{J}\sqrt{u_1'^2 + u_2'^2}$ of (d).

As Fig. 1 shows, the design starts from a rectangular virtual space filled with homogeneous and isotropic material. This virtual space (described by the point $Z = x_1 + \mathrm{i}x_2$ of the complex plane) is transformed into a semicircular ring-shaped physical space (described by the point $z = x'_1 + \mathrm{i}x'_2$) with the conformal mapping $z = e^Z$. In this case, we have

$$J = \frac{x_1^2 + x_2^2}{\Delta^2} = \frac{r^2}{\Delta^2}, \tag{9}$$

$$\left\langle \frac{\partial x'_r}{\partial x_k}\frac{\partial x'_s}{\partial x_l}\right\rangle \sim J, \quad \left\langle \frac{\partial^2 x'_i}{\partial x_k \partial x_l}\right\rangle \sim \frac{\sqrt{2}r}{\Delta^2}, \tag{10}$$

where $\Delta = 1$ m to make J dimensionless. Consequently, Eq. (6) becomes

$$\eta = \frac{\pi^2 r^2}{L'^2 + 2\sqrt{2}\pi r L'}\left(\frac{C'_p}{C'_s}\right)^2. \tag{11}$$

To ensure a sufficiently large η, we set $\rho = 1000$ kg/m^3, $\lambda = 673.91$ MPa, and $G = 0.07$ MPa. According to Eq. (8), material properties of this semicircular ring in the physical space are

$$\lambda' = \frac{r^2}{\Delta^2}\lambda, \quad G' = \frac{r^2}{\Delta^2}G, \quad \rho' = \rho, \quad \mu' = \mu. \tag{12}$$

Since $C'_p = \sqrt{(\lambda' + 2G')/\rho'} = C_p r/\Delta$, and $C'_s = \sqrt{G'/\rho'} = C_s r/\Delta$, it is easy to verify that a large η can be easily achieved.

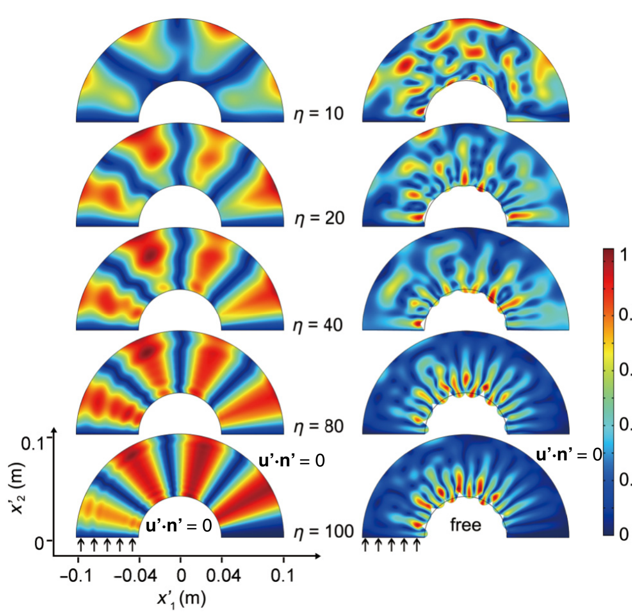

FIG. 2. Snap shots of the modified total displacement $\sqrt{J}\sqrt{u_1'^2 + u_2'^2}$ (normalized to the amplitude of the incident wave) for different η simulated by COMSOL MULTIPHYSICS.

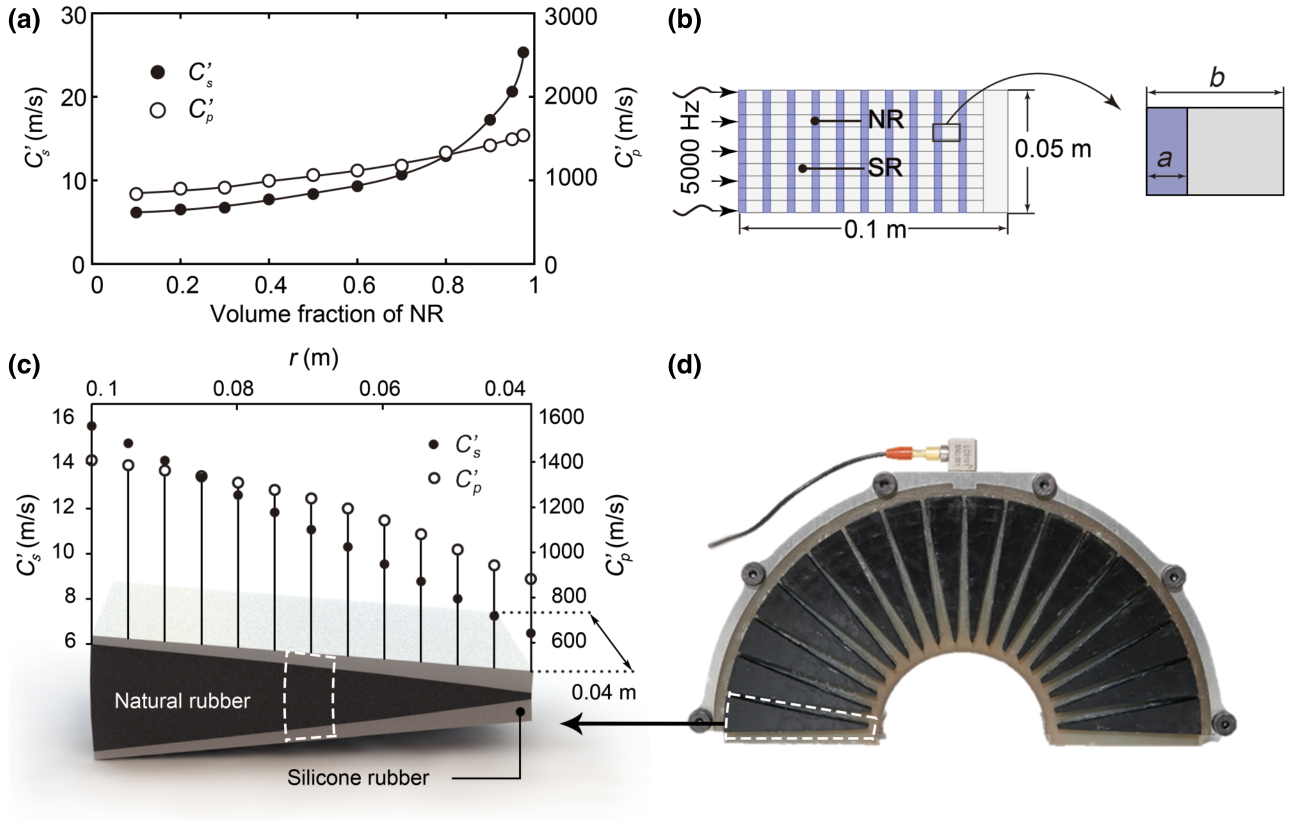

FIG. 3. (a) Effective wave velocities obtained from finite element models with different volume fractions of NR, which is solved by COMSOL MULTIPHYSICS. (b) Model of the rectangular domain containing 100 cells with the incident wave from the left side and the details of one cell composed of two kinds of rubber. (c) The fan cell and the distribution of effective wave velocities C_p' and C_s'. (d) The vibration isolator with inside wave bender and outside aluminum shell.

With these material properties, we conduct numerical simulations with pure sinusoidal incident longitudinal waves to check the wave-bending effect with the help of the COMSOL MULTIPHYSICS. The polarization of the source is perpendicular to the excitation face as denoted by the arrows. $\mathbf{u}\cdot\mathbf{n}=0$ and $\mathbf{u}'\cdot\mathbf{n}'=0$ denote the normal constraints on the boundaries in virtual space and the physical space, respectively. The boundary opposite to the excitation face is set to be a "low reflecting boundary" in COMSOL MULTIPHYSICS. In Fig. 1(a), since the upper and lower boundaries are normally constrained, only pure longitudinal waves propagate in virtual space. As Fig. 1(c) shows, the wave does bend in the corresponding physical space with the displacement magnitude inversely proportional to r. This coincides with the relation $u_i = u_j' \, \partial x_j'/\partial x_i$. Since the incident waves pass along the tangent direction of the outer boundary rather than transmitting through its normal direction, the supported object (denoted by a little square on the top) will not be disturbed. In this way, this wave bender can be used as an alternative vibration isolator. In addition, since $\langle u_i\rangle \sim \langle u_j'\rangle\langle \partial x_j'/\partial x_i\rangle \sim \sqrt{J}\langle u_j'\rangle$, the modified total displacement $\sqrt{J}\sqrt{u_1'^2+u_2'^2}$ can better illustrate the wave-bending effect after the transformation.

The η in Eq. (11) is a crucial index that measures the performance of this wave bender. We can increase η by using a material with a large ratio of $C_p'/C_s' = \sqrt{\lambda'/G'+2}$. Since $\lambda' = E'\nu'/[(1+\nu')(1-2\nu')]$ and $G' = E'/[2(1+\nu')]$ (E' is the Young's modulus and ν' is the Poisson's ratio), the ratio of $C_p'/C_s' = \sqrt{2\nu'/(1-2\nu')+2}$ can be maximized when $\nu' \to 0.5$. Therefore, it is a natural choice to use rubbers to fabricate this isolator. Eq. (11) also implies that we should decrease the wavelength L'. For this purpose, it is preferable to convert the elastic waves into surface modes, for example, the wavelength of the Rayleigh wave is slightly smaller than the transverse wave [30] and much smaller than the longitudinal wave at the same frequency. The wave-mode conversion can be achieved by releasing the normal constraint on the boundary, where most waves concentrate near the free surface in the Rayleigh mode (see Figs. 1(b), 1(d) and 1(f) and Fig. S1 within the Supplemental Material [31]).

To check the impact of η on the performance of this wave bender, we compare the wave-bending effects for different η in Fig. 2. In the simulation, C_p'/C_s' is in the range of 9.8–31.0, while the wave frequency f is adjusted to keep a constant wavelength of $L' = \pi r/2$ in order to ensure clear comparisons. In this way, η is in the range

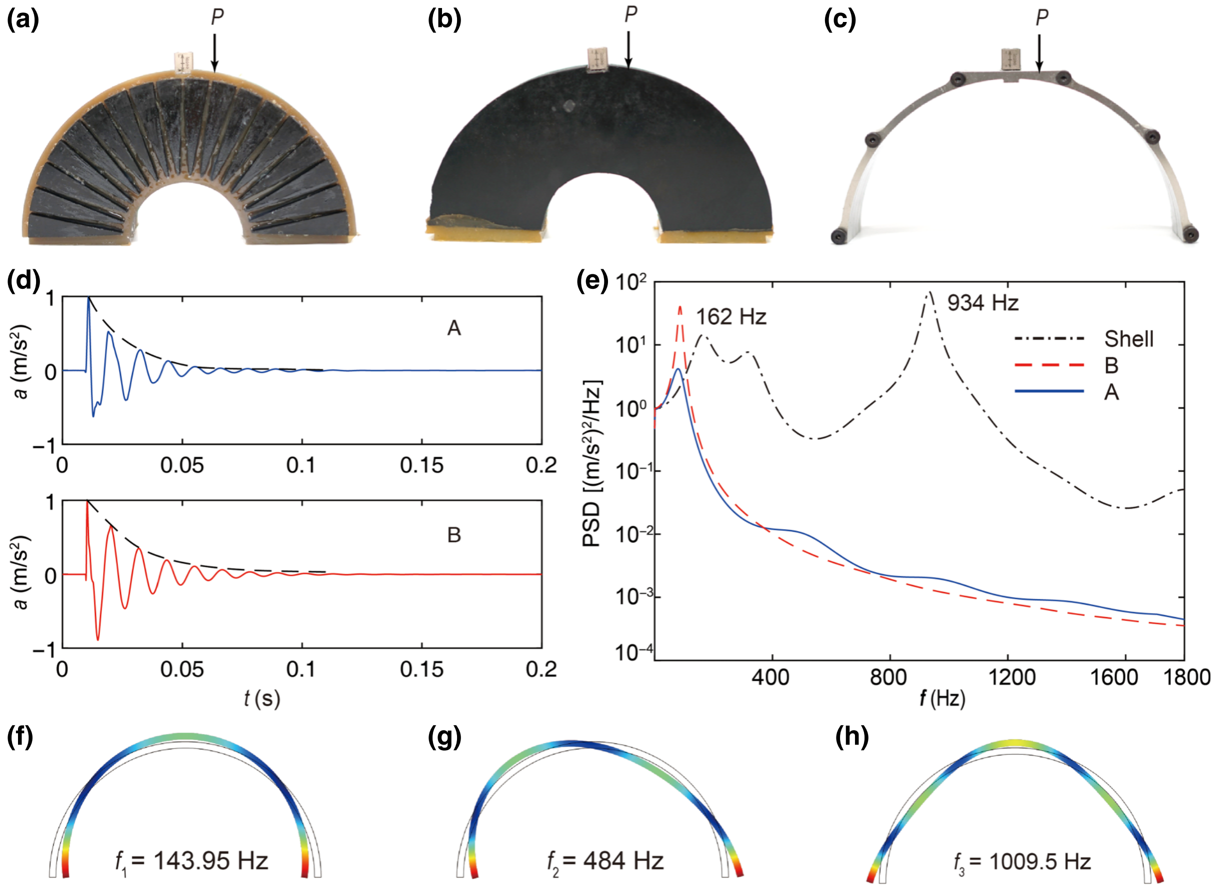

FIG. 4. (a) Free vibration test of the wave bender. (b) Free vibration test of the pure rubber. (c) Free vibration test of the aluminum shell. (d) Acceleration signals on the top of the wave bender (A) and the pure rubber (B), normalized to the maximum amplitude of the pulse P. (e) Power spectrum density of the acceleration signals. (f), (g), (h) First three vibration modes of the aluminum shell solved by the COMSOL MULTIPHYSICS.

of 10–100 according to Eq. (11). The simulation results approximately indicate that good bending effects can be achieved when $\eta > 80$. This means that when the extra term is two orders smaller than other terms, the elastic wave equations are nearly form invariant.

B. Fabricating the vibration isolator

The effective material properties of this wave bender given in Eq. (12) can be easily realized because they are isotropic. A simple way is mixing two kinds of conventional rubbers inside a representative cell (see Fig. 3).

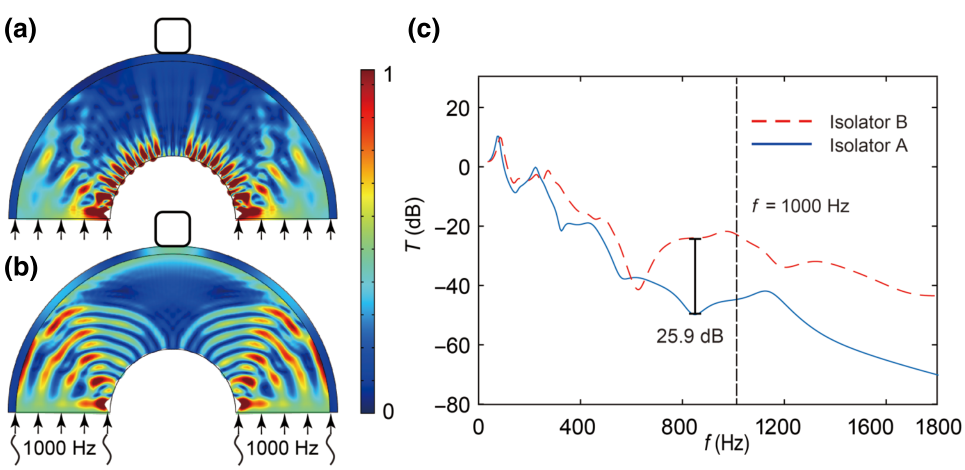

FIG. 5. (a) Snap shot of the total displacement field $\sqrt{u_1'^2 + u_2'^2}$ (normalized to the amplitude of the incident wave) of isolator A at 1000 Hz. (b) Snap shot of the total displacement field $\sqrt{u_1'^2 + u_2'^2}$ (normalized to the amplitude of the incident wave) of isolator B at 1000 Hz. (c) Transfer functions of isolator A and isolator B.

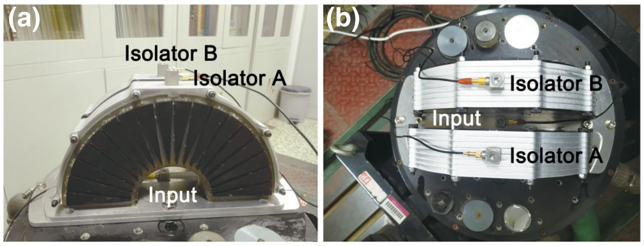

FIG. 6. The setup of the shaking table test. (a) Front view. (b) Top view.

The material properties of two rubbers adopted here are as follows: natural rubber (NR) $E'_{\mathrm{NR}} = 2.61$ MPa, $\rho'_{\mathrm{NR}} = 1003$ kg/m^3, $C'_{p(\mathrm{NR})} = 1592$ m/s; silicone rubber (SR) $E'_{\mathrm{SR}} = 0.11$ MPa, $\rho'_{\mathrm{SR}} = 1092$ kg/m^3, $C'_{p(\mathrm{SR})} = 821$ m/s. Since the small difference of densities can be neglected compared with the huge difference of stiffness for these two kinds of rubbers, we can focus on realizing λ' and G' at different r. This can be achieved by adjusting the volume fraction ratio of NR inside a cell at different r [see Fig. 3(c)].

The relations between effective wave velocities and the volume fraction of NR are obtained by numerical simulations solved by COMSOL MULTIPHYSICS. A rectangular domain containing 100 cells is used in the simulation in Fig. 3(b). Each cell is 10×5 mm^2 and consists of two different kinds of rubbers mentioned above. The volume fraction of NR is defined as a/b, and it varies from 0.1 to 0.95. For the simulation using longitudinal incident waves at frequency 5000 Hz, the upper and lower boundaries are normally constrained. While for the simulation using shear waves, tangential displacements are constrained on the upper and lower boundaries, and the frequency is set to be 100 Hz. The obtained relations between effective wave velocities and the volume fraction of NR are plotted in Fig. 3(a), which indicates that wave velocities (especially the shear velocity) are almost proportional to the volume fraction of NR in the range of 0.0–0.8. The relations at other frequencies are almost the same as those in Fig. 3(a) (see Fig. S2 in Ref. [31]).

Based on Fig. 3(a), we can design the internal structures of the wave bender with an inner radius of 0.04 m and an outer radius of 0.1 m [see Fig. 3(c)]. To facilitate load bearing, the thickness of this bender is set to be 0.04 m. 18 evenly distributed fan cells are in charge of wave bending. Inside each fan cell, there are 13 pairs of points on the two interfaces between NR and SR and they are evenly distributed along the radius. The circumferential distance of each pair of points determines the volume fraction of NR at position r. This distance is determined by the shear velocity curve in Fig. 3(a) to guarantee that C'_s is strictly proportional to r. Applying the curve fitting through these 13 pairs of points obtains the two interfaces between NR and SR. As Fig. 3(c) shows, $C'_p = 1390$ m/s and $C'_s = 15.5$ m/s on the outer boundary. Referring to Fig. 2, if we require $\eta > 80$ to ensure the bending performance, L' on the outer boundary should be less than 2.74 m according to Eq. (11). This implies that the effective bending of longitudinal waves on the outer boundary approximately starts from the frequency of 507 Hz.

To ensure the integrity of this wave bender, there remain two margins of SR in 5-mm thicknesses on the inner and outer boundaries [see Fig. 3(d)]. This does not affect its vibration isolation performance because waves have already been bent inside the wave bender.

The final assembly of the vibration isolator has a 6061 aluminum alloy shell with a 5-mm thickness on the outer boundary of this wave bender. Since the acoustic impedance of the aluminum shell is much larger than that of the rubber, the shell can be used as the normal constraint required on the outer boundary of the wave bender [see Fig. 1(d)]. In addition, the silicone oil with a viscosity of 350 cs is used to lubricate the interface between the shell and the rubber, so that the shear force on the interface can be reduced.

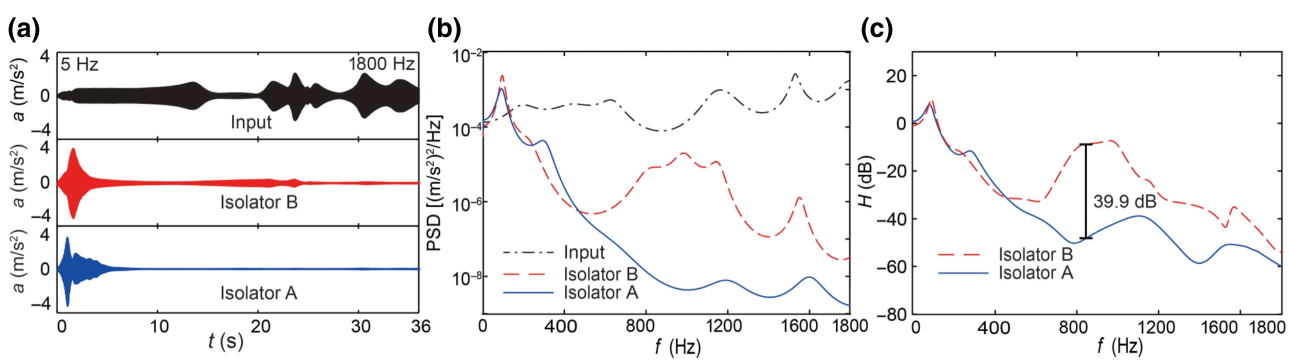

FIG. 7. Results of the sweep frequency test. (a) Accelerations measured on the aluminum base (input), the top of isolator B, and the top of isolator A. (b) The power spectrum density of the accelerations. (c) The transmissibility of isolator A and isolator B.

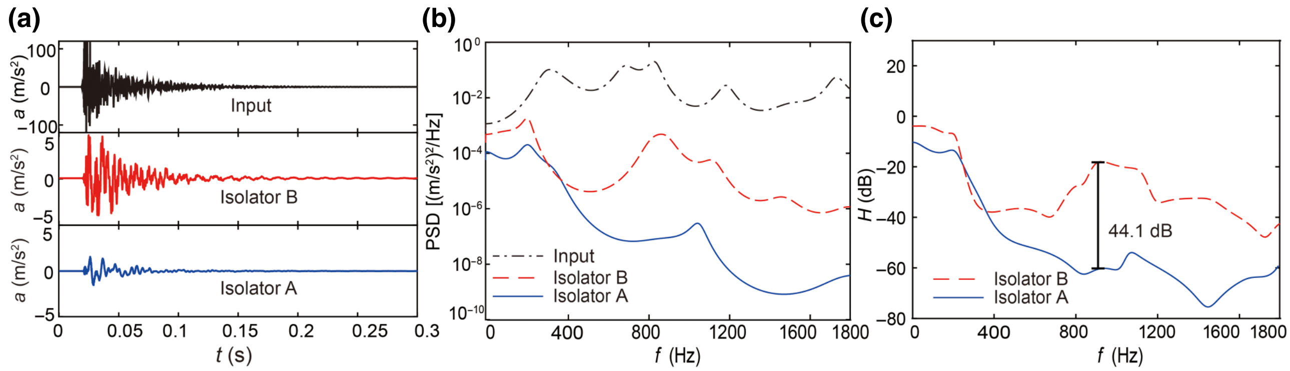

FIG. 8. Results of the tap test. (a) Accelerations measured on the aluminum base (input), the top of isolator B, and the top of isolator A. (b) The power spectrum density of the accelerations. (c) The transmissibilities of isolator A and isolator B.

IV. EXPERIMENTS

A. Basic properties of specimens

To test the performance of the isolator fabricated in Sec. III (denoted as isolator A), we compare it with another isolator of the same shape (denoted as isolator B). Both isolators have the same aluminum shell, but in contrast to isolator A, isolator B replaces the wave bender [see Fig. 4(a)] with a pure NR of $E = 1.12$ MPa and $\rho = 1072$ kg/m^3 [see Fig. 4(b)]. A layer of SR is attached at the bottom of the NR in isolator B so that the measured static support stiffnesses of these two isolators are almost the same (71,428 N/m for isolator A and 76,923 N/m for isolator B).

Since the damping has a great impact on the vibration isolation performance, we also measure the damping ratio by using the free vibration test. As Figs. 4(a) and 4(b) show, low frequency pulses indicated by P are applied on the top of the wave bender and the pure NR with a rubber hammer. The damping ratio ς and the resonance frequency f_n can be extracted from the signals in the time domain [see Fig. 4(d)] as $f_{n(A)} = 76$ Hz, $f_{n(B)} = 85$ Hz, $\varsigma_A = 0.1039$, and $\varsigma_B = 0.1013$. The conclusion of $\varsigma_B < \varsigma_A$ can also be confirmed in Fig. 4(e), because the peak at $f_{n(A)}$ is lower than that at $f_{n(B)}$. The result of the free vibration test for the aluminum shell is also presented in Fig. 4(e), in which we can find two dominant f_n at 162 and 934 Hz, which coincide with the first and the third f_n simulated by COMSOL MULTIPHYSICS [Figs. 4(f) and 4(h)].

B. Simulation results

Before the real testing, the performances of these two isolators are simulated by using the COMSOL MULTIPHYSICS. Since it is very difficult to accurately determine the damping inside the complex assembly of these isolators, we use the same damping ratio of 0.1 in the simulations. "The Thin Elastic Layer boundary condition" in COMSOL MULTIPHYSICS with normal stiffness of $k_n = 1 \times 10^{13}$ N/m^2 and tangent stiffness of $k_t = 0$ N/m^2 is used on the interface between the shell and rubber.

As Fig. 5(a) shows, most of the incident waves are converted into the Rayleigh mode and bent along the inner boundary of isolator A, so that there is little disturbance on the aluminum shell. While as Fig. 5(b) shows, a large fraction of waves directly transmits through the aluminum shell of isolator B, so that it could have poorer isolation performance than that of isolator A. These observations can be further confirmed in Fig. 5(c), where the transfer function of isolator A has the maximum reduction of 25.9 dB at 853 Hz. The transfer function is defined as $T(f) = 20\log_{10}[u_{\text{top}}(f)/u_{\text{input}}(f)]$, where $u_{\text{input}}(f)$ and $u_{\text{top}}(f)$ are the amplitudes of incident waves and the top of isolators at frequency f, respectively.

C. Experimental results

As Fig. 6 shows, a shaking table test with sweep frequency input signals is first conducted to test the real performances of these two isolators. These isolators are placed close on an aluminum base mounted on a shaking table. An accelerator is fixed in the center of the aluminum base to measure the input signal generated by the shaking table. Two other identical accelerators are fixed on top of isolator A and isolator B, respectively. The recorded accelerations are plotted in Fig. 7(a), which shows the obvious reduction of amplitude by using isolator A. More detailed comparisons are given in Fig. 7(c). The transmissibility is defined as $H(f) = 10\log_{10}[X_T(f)/X_I(f)]$, where X_T denotes the power spectrum density of the acceleration measured on the top of isolator A or B, and X_I denotes the power spectrum density of the input acceleration measured on the aluminum plate. Since isolator A has little bit larger damping ratio than that of isolator B as we measured in Fig. 4, its transmissibility around resonance is smaller than that of isolator B. According to the traditional passive isolation theory [32], isolator A should be less effective than isolator B at frequencies above the resonance. However, as Fig. 7(c) shows, after $f > 483$ Hz, isolator A surpasses isolator B and achieves its best performance at $f = 833$ Hz with a 39.9-dB further reduction of transmissibility. These observations are consistent with the estimation of the starting frequency of 507 Hz given in Sec. II B and the best performance frequency of 853 Hz given in Fig. 5(c). In addition, the bending effect disappears at high frequencies. This is because compared with the circumferential size of a cell, the wavelengths are not large enough to ensure the effective wave velocities.

Besides the sweep frequency test, the tap test is also conducted for comparison. In the tap test, the positions of two isolators and three accelerators are the same as those of the sweep frequency test (see Fig. 6). An input signal is generated by tapping on the aluminum base using a steel hammer. The recorded signals are plotted in Fig. 8(a), which confirms that isolator A outperforms isolator B. A detailed comparison in the frequency domain is presented in Fig. 8(c). Similar to the sweep frequency test, after $f > 387$ Hz, isolator A surpasses isolator B and achieves its best performance at $f = 910$ Hz with a 44.1-dB further reduction of transmissibility. However, we cannot find peaks at resonant frequencies, because the input signal due to tapping is mainly at high frequencies, so that the power around f_n is not high enough to excite the resonance of the isolators.

V. SUMMARY

In this paper, we propose a general method to design elastic metamaterials based on the conformal transformation. The great challenge of form invariance is solved by using a material whose longitudinal wave velocity is much larger than the transverse wave velocity. In addition, the performance of the resultant elastic metamaterial can be further improved by introducing interfaces to convert elastic waves into the modes with short wavelengths. The validity of this design method is demonstrated by an elastic wave bender acting as a vibration isolator. Although this is a simple example, it shows a superior performance at broad frequency bandwidth and even breaks the limit on damping ratios required by the classic passive vibration theory. Thus, we can envisage that other interesting implementations of elastic metamaterials can be achieved in the future by using the method proposed in this paper.

ACKNOWLEDGMENTS

This work was supported by the National Natural Science Foundation of China with Grant No. 11672144. The assistance of B. Wang and Q. H. Lu for the shaking table test is greatly appreciated.

[1] J. B. Pendry, D. Schurig, and D. R. Smith, Controlling electromagnetic fields, Science **312**, 1780 (2006).

[2] U. Leonhardt, Optical conformal mapping, Science **312**, 1777 (2006).

[3] S. A. Cummer and D. Schurig, One path to acoustic cloaking, New J. Phys. **9**, 45 (2007).

[4] H. Chen and C. T. Chan, Acoustic cloaking in three dimensions using acoustic metamaterials, Appl. Phys. Lett. **91**, 183518 (2007).

[5] M. Farhat, S. Enoch, S. Guenneau, and A. B. Movchan, Broadband Cylindrical Acoustic Cloak for Linear Surface Waves in a Fluid, Phys. Rev. Lett. **101**, 134501 (2008).

[6] S. Zhang, D. A. Genov, C. Sun, and X. Zhang, Cloaking of Matter Waves, Phys. Rev. Lett. **100**, 123002 (2008).

[7] D. Schurig, J. J. Mock, B. J. Justice, S. A. Cummer, J. B. Pendry, A. F. Starr, and D. R. Smith, Metamaterial electromagnetic cloak at microwave frequencies, Science **314**, 977 (2006).

[8] R. Liu, C. Ji, J. J. Mock, J. Y. Chin, T. J. Cui, and D. R. Smith, Broadband ground-plane cloak, Science **323**, 366 (2009).

[9] P. Ball, Bending the laws of optics with metamaterials: An interview with John Pendry, Natl. Sci. Rev. **5**, 200 (2018).

[10] S. Zhang, C. Xia, and N. Fang, Broadband Acoustic Cloak for Ultrasound Waves, Phys. Rev. Lett. **106**, 024301 (2011).

[11] G. Ma and P. Sheng, Acoustic metamaterials: From local resonances to broad horizons, Sci. Adv. **2**, e1501595 (2016).

[12] W. S. Gan, *New Acoustics Based on Metamaterials* (Springer, Singapore, 2018).

[13] G. W. Milton, M. Briane, and J. R. Willis, On cloaking for elasticity and physical equations with a transformation invariant form, New J. Phys. **8**, 248 (2006).

[14] M. Brun, S. Guenneau, and A. B. Movchan, Achieving control of in-plane elastic waves, Appl. Phys. Lett. **94**, 061903 (2009).

[15] A. N. Norris and A. L. Shuvalov, Elastic cloaking theory, Wave Motion **48**, 525 (2011).

[16] J. Hu, Z. Chang, and G. Hu, Approximate method for controlling solid elastic waves by transformation media, Phys. Rev. B **84**, 201101(R) (2011).

[17] Z. Chang, Jin Hu, Gengkai Hu, Ran Tao, and Yue Wang, Controlling elastic waves with isotropic materials, Appl. Phys. Lett. **98**, 121904 (2011).

[18] M. Farhat, S. Guenneau, and S. Enoch, Ultra Broadband Elastic Cloaking in Thin Plates, Phys. Rev. Lett. **103**, 024301 (2009).

[19] N. Stenger, M. Wilhelm, and M. Wegener, Experiments on Elastic Cloaking in Thin Plates, Phys. Rev. Lett. **108**, 014301 (2012).

[20] M. Dubois, M. Farhat, E. Bossy, S. Enoch, S. Guenneau, and P. Sebbah, Flat lens for pulse focusing of elastic waves in thin plates, Appl. Phys. Lett. **103**, 071915 (2013).

[21] J. Zhu, Yongquan Liu, Zixian Liang, Tianning Chen, and Jensen Li, Elastic Waves in Curved Space: Mimicking a Wormhole, Phys. Rev. Lett. **121**, 234301 (2018).

[22] W. J. Parnell, A. N. Norris, and T. Shearer, Employing pre-stress to generate finite cloaks for antiplane elastic waves, Appl. Phys. Lett. **100**, 171907 (2012).

[23] D. J. Colquitt, M. Brun, M. Gei, A. B. Movchan, N. V. Movchan, and I. S. Jones, Transformation elastodynamics and cloaking for flexural waves, J. Mech. Phys. Solids **72**, 131 (2014).

[24] Z. H. Xiang, The form-invariance of wave equations without requiring a priori relations between field variables, Sci. China Phys. Mech. Astron. **57**, 2285 (2014).

[25] S. Brûlé, E. H. Javelaud, S. Enoch, and S. Guenneau, Experiments on Seismic Metamaterials: Molding Surface Waves, Phys. Rev. Lett. **112**, 133901 (2014).

[26] M. K. Lee and Y. Y. Kim, Add-on unidirectional elastic metamaterial plate cloak, Sci. Rep. **6**, 20731 (2016).

[27] U. Leonhardt and T. Philbin, *Geometry and Light* (Dover, New York, 2010), pp. 166–170, 173–175.

[28] G. D. Manolis, T. V. Rangelov, and R. P. Shaw, Conformal mapping methods for variable parameter elastodynamics, Wave Motion **36**, 185 (2002).

[29] P. J. Olver, in *Equivalence, Invariants, and Symmetry* (Cambridge University Press, Cambridge, 1995), pp. 221–251.

[30] J. L. Rose, in *Ultrasonic Guided Waves in Solid Media* (Cambridge University Press, Cambridge, 2014), pp. 108–119.

[31] See Supplementary Material at http://link.aps.org/supplemental/10.1103/PhysRevApplied.11.064040 for the close-up view of the Rayleigh waves inside in figure S1, and the relation of the longitudinal wave velocity to the volume fraction of natural rubber at frequencies from 1000 Hz to 5000 Hz in figure S2.

[32] H. LeKuch, in *Harris Shock and Vibration Handbook*, edited by A. G. Piersol and T. L. Paez (McGraw-Hill, New York, 2009), ed. 6, pp. 39.5–39.6.